

POTR: Post-Training 3DGS Compression

Bert Ramlot , Martijn Courteaux , Peter Lambert , *Senior Member, IEEE*,
Glenn Van Wallendael , *Member, IEEE*

Abstract—3D Gaussian Splatting (3DGS) has recently emerged as a promising contender to Neural Radiance Fields (NeRF) in 3D scene reconstruction and real-time novel view synthesis. 3DGS outperforms NeRF in training and inference speed but has substantially higher storage requirements. To remedy this downside, we propose POTR, a post-training 3DGS codec built on two novel techniques. First, POTR introduces a novel pruning approach that uses a modified 3DGS rasterizer to efficiently calculate every splat’s individual removal effect simultaneously. This technique results in 2-4 \times fewer splats than other post-training pruning techniques and as a result also significantly accelerates inference with experiments demonstrating 1.5-2 \times faster inference than other compressed models. Second, we propose a novel method to recompute lighting coefficients, significantly reducing their entropy without using any form of training. Our fast and highly parallel approach especially increases AC lighting coefficient sparsity, with experiments demonstrating increases from 70% to 97%, with minimal loss in quality. Finally, we extend POTR with a simple fine-tuning scheme to further enhance pruning, inference, and rate-distortion performance. Experiments demonstrate that POTR, even without fine-tuning, consistently outperforms all other post-training compression techniques in both rate-distortion performance and inference speed.

Index Terms—3DGS, compression, spherical harmonics, energy compaction, pruning.

I. INTRODUCTION

Synthesizing new views from a limited number of camera-captured images is a long-standing problem in computer graphics [1]–[3]. Various techniques have been proposed to address this challenge, focusing on multiview video coding [4], [5], cross-view image matching [6], sparse compact representations [7], and real-time VR experiences [8], [9]. Among the most promising solutions are Neural Radiance Fields (NeRF) [10] and 3D Gaussian Splatting (3DGS) [11]. While NeRF has seen substantial year-over-year improvements [12]–[14], 3DGS achieves better training and inference speeds through a scene representation based on feature-rich volumetric points called *splats*. This alternate representation is also the culprit behind 3DGS’s biggest comparative downside to NeRF, namely, substantially higher storage requirements. For example, a simple unbounded scene with a central object typically results in a model size of 0.3-1.5 GB, often making

This work was funded in part by the Research Foundation—Flanders (FWO) under Grant 1SA0B26N, the imec.prospect project SitSens, ID-Lab (Ghent University—imec), Flanders Innovation and Entrepreneurship (VLAIO), and the European Union.

The authors are with the IDLab-MEDIA research group, part of Ghent University and imec, located at AA Tower, Technologiepark-Zwijnaarde 122, B-9052 Zwijnaarde, Belgium. Corresponding author: Bert Ramlot. (e-mail: bert.ramlot@ugent.be; martijn.courteaux@ugent.be; peter.lambert@ugent.be; glenn.vanwallendael@ugent.be).

This work has been submitted to the IEEE for possible publication. Copyright may be transferred without notice, after which this version may no longer be accessible.

transfer and storage challenging, particularly for on-demand applications. Furthermore, with 3DGS literature expanding toward larger scenes [15], [16] and immersive video [17], [18], 3DGS compression is becoming increasingly important.

The literature has recognized the need for compression through numerous 3DGS-specific compression techniques [19]–[51], most of whom are *in-training* compression techniques [19]–[44] that alter the training process to achieve smaller models. While this works well, this level of control over the training process is not guaranteed as one might want to re-encode an existing 3DGS model, similarly to how videos and images are re-encoded. To this end, a fraction of the 3DGS compression literature focuses on *post-training* compression [45]–[51] as they start from an existing model. Lack of control over the training process generally results in poorer rate-distortion (RD) performance. As a result, post-training compression approaches commonly incorporate a fine-tuning step to somewhat level the playing field. This step further trains the already trained model to recover some of the quality lost during compression. Although this is a powerful way for a post-training codec to utilize the extra flexibility offered by the in-training compression paradigm, it side-steps the issue of *post-training* compression. Nevertheless, current post-training methods primarily focus on RD performance after fine-tuning.

To this end, we propose **POTR**, a **post-training** 3DGS codec that focuses predominantly on achieving strong RD performance without any fine-tuning. POTR significantly outperforms existing post-training methods, achieving up to a fourfold reduction in model size compared to the previous state-of-the-art. Additionally, our compressed models use far fewer splats and therefore render faster. This markedly better performance is achieved through two novel compression techniques.

Our first novel technique introduces a new approach to splat removal. Where existing post-training pruning methods rely on heuristics involving metrics such as a splat’s size, opacity, and importance, we propose a pruning technique that directly evaluates the impact of removing each splat on an objective quality metric. This approach allows our high-quality compressed models to use 2–4 \times fewer splats than other post-training methods across four common datasets. Additionally, our pruning method significantly accelerates inference, often achieving at least 50% higher frames per second. At higher distortion levels, the performance gap widens further, with experiments showing examples of 2 \times higher frame rates than other post-training compressed models.

Our second novel technique focuses on spherical harmonics coefficients — commonly referred to as lighting coefficients — which represent a splat’s view-dependent color. Lighting

coefficients constitute over 80% of the uncompressed model’s size, making them vital to compression. To address this, we first represent a splat’s colors for all training views using a single linear system. Next, we introduce a spherical harmonics energy compaction method that uses a heavily modified version of ridge regression to compute an alternate set of lighting coefficients. These new coefficients exhibit significantly lower entropy while producing nearly identical colors for relevant training views and generalizing better to novel views. Combined with quantization and entropy compression, we demonstrate that lighting coefficients are no longer the largest contributor to model size using our spherical harmonics energy compaction method. To our knowledge, this is the first post-training 3DGS compression method to non-trivially recompute lighting coefficients without any form of training.

In summary, the main contributions of this paper are:

- Proposing an efficient method to evaluate the impact of removing each splat on an objective quality metric. Use this to design a pruning strategy that significantly outperforms other post-training methods in both RD performance and inference speed, particularly at higher distortion levels.
- Introducing a fast, systematic approach to transform high-entropy spherical harmonics coefficients into low-entropy ones while preserving the splat’s colors for relevant training views. Our method requires no training, is embarrassingly parallel, and improves generalization.
- Developing POTR, a fine-tuneless post-training codec that leverages the above two techniques to achieve state-of-the-art RD performance and inference speed, surpassing all other (fine-tuning-based) post-training methods. Additionally, we demonstrate that extending POTR with a simple fine-tuning scheme further enhances RD performance and inference speed.

The remainder of this work is organized as follows. Section II briefly overviews the relevant literature. Next, Section III discusses the necessary background on 3DGS which will be used extensively in Section IV which provides a detailed description of our proposed compression methods and codec. Section V presents our results, experiments, and associated discussions. Finally, Section VI summarizes this work.

II. RELATED WORK

A. NeRF compression

Voxel-based techniques are a popular solution for enhancing the training and rendering speeds of NeRFs [52], [53]. However, these methods often lead to large storage overhead, for example, KiloNeRF [53] necessitates the storage of thousands of neural networks. As a result, a large fraction of the NeRF compression literature focuses on voxel-based techniques. Voxel-based techniques are comparable to 3DGS in that their representation is more localized. This localization generally eases compression as it improves existing, or allows for new, compression techniques such as voxel pruning [54]–[56], transform coding [56]–[61], various forms of quanti-

zation [55], [62], [63], and specialized context models for entropy compression [64].

B. Point-cloud compression

Point-cloud geometry is commonly compressed using octrees [65]–[67]. The octree structure is serialized by encoding the occupancy bits of the octree’s nodes, which are subsequently compressed using entropy coding. To achieve higher compression ratios, several custom entropy models have been proposed. Examples include a tree-structured entropy model utilizing MLPs [67], an intra-prediction-based entropy model [65], and a deep entropy model [66].

The compression of point-cloud attributes, such as color values and normal vectors, is another key area of research [68]. While fully 3D methods often use octrees to encode attributes [69]–[71], alternative approaches where 3D data is mapped onto 2D planes, allowing the use of standard image and video compression techniques [72], do occur.

C. 3D Gaussian Splatting compression

To address 3DGS’s stringent storage requirements, several compression techniques have been proposed [19]–[51]. Early approaches are comprehensively surveyed in 3DGS.zip [73], which also introduces a methodology to compare different 3DGS compression techniques. Notably, the 3DGS literature bears close resemblance to point-cloud compression literature by, for example, compressing splat geometry using octrees [28], [46] and projecting 3D attributes onto 2D planes to allow for image-based compression [20]–[22]. Some works even directly use point cloud codecs, for example, G-PCC [23], [24], [26], [43], [50]. While point-cloud-inspired techniques result in substantial RD gains, the largest gains of the 3DGS literature originate from 3DGS-specific techniques.

A first group of 3DGS-specific compression techniques focuses on reducing the number of splats. Most approaches assign each splat a heuristic score, computed using factors such as sensitivity [47], opacity [22]–[26], [30], [44], [45], importance [29], [38], [41], [46], intersection [37], [41], maximum contribution [38], [40], uncertainty [39], [49] or volume [45], [46], [50]. Splats with scores below a chosen threshold are then removed [22]–[26], [29], [30], [33], [45]–[47]. Another more indirect approach is to apply a downward pressure on the number of splats during training by altering the loss function [19], [25]–[28], [31], [32], [34], [35], [40], [42]. Both methods have been quite successful at reducing the number of splats, so much so that the largest inference time improvements have thus far originated from the compression literature, highlighting its contribution to Gaussian Splatting beyond size reduction.

A second group of 3DGS-specific compression techniques addresses the substantial storage requirements of lighting information. In 3DGS’s original formulation, lighting information is modeled using spherical harmonics (SH) and their coefficients. The latter are stored and account for over 80% of all attributes, leading some works to avoid explicitly saving lighting coefficients altogether. Instead, latent attributes are stored and processed using an MLP to generate either direct

color outputs [23]–[26], [30], [31], [34], [36], [42], or lighting coefficients [20], [21], [29], [32]. For methods that store the lighting coefficients explicitly, additional techniques are applied to lower the lighting coefficients’ entropy. Examples include trainable masks [28], [35], SH band pruning after densification [33], distillation of higher-degree SH terms to lower degrees [45], and transformations such as Region-Adaptive Hierarchical Transform [37], [46] and JPEG XL [22].

To summarize, a range of techniques are used to compress 3DGS models, but those that focus on reducing the number of splats or compressing lighting information are the most crucial to achieving strong RD performance. Compressing other properties — such as position, scale, rotation, and opacity — is comparatively less important, as these contribute only a small portion to the overall uncompressed size. Moreover, reducing the number of splats not only enhances RD performance but also boosts inference speed, underscoring the importance of compression techniques beyond just storage efficiency.

III. 3D GAUSSIAN SPLATTING

3DGS models consist of a collection of splats, each with a center $\mu \in \mathbb{R}^3$ in space. For a point in space $\mathbf{p} \in \mathbb{R}^3$, the splat’s density is proportional to a 3D Gaussian with a covariance matrix $\Sigma \in \mathbb{R}^{3 \times 3}$:

$$\mathcal{G}(\mathbf{p}) = \exp\left(-\frac{1}{2}(\mathbf{p} - \mu)^T \Sigma^{-1}(\mathbf{p} - \mu)\right). \quad (1)$$

To render a 3DGS model for a given camera, a splat’s density is first projected into screen space. This is done efficiently using the affine invariance of multivariate Gaussians by approximating the projective transformation as an affine transformation. The resulting 2D density is therefore again proportional to a 2D Gaussian and denoted as \mathcal{G}^{2D} . Next, the splats are alpha-composited by associating each splat with a layer and ordering these layers according to the splats’ approximate depth. Upon rasterizing a splat’s layer, a pixel at position $\mathbf{x} \in \mathbb{R}^2$ has an opacity

$$\alpha = o \cdot \mathcal{G}^{2D}(\mathbf{x}), \quad (2)$$

where o represents the location-independent base opacity of the splat. The yet undetermined fraction of a pixel’s color after alpha compositing the first k layers is termed the transmittance and is defined as

$$T_k = \prod_{j=0}^{k-1} (1 - \alpha_j). \quad (3)$$

After alpha-compositing all K visible splats over a black background, the final color of a pixel located at $\mathbf{x} \in \mathbb{R}^2$ is given by

$$\mathbf{c}(\mathbf{x}) = \sum_{k=0}^{K-1} T_k \alpha_k \mathbf{c}_k \quad (4)$$

where \mathbf{c}_k is the color of the k -th splat in the alpha compositing process.

While a splat’s color is monochromatic across the pixels of a still frame, it is view-dependent based on the camera’s position through a spherical function defined using real spherical harmonics. 3DGS’s original formulation uses all real

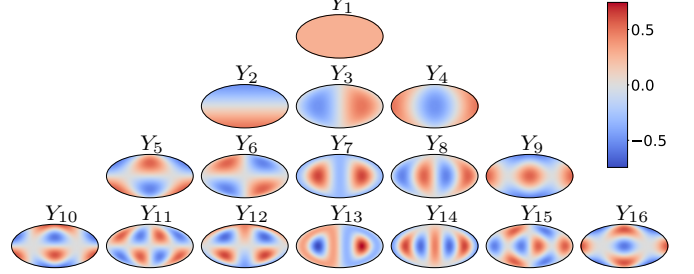


Fig. 1: Mollweide projection of the first 16 real spherical harmonics.

spherical harmonics with a degree $l \leq 3$, all of whom are shown in Figure 1. To ease iterating these functions, each degree-order pair (l, m) is mapped to a unique index using $(l, m) \rightarrow l(l+1) + m + 1$. The first spherical harmonic Y_1 is often singled out and called the DC spherical harmonic as it is the only basis that is view-independent and the only basis that is not zero-meanned. All other spherical harmonics are called AC spherical harmonics. The value of a splat’s color channel is determined by the M lighting coefficients associated with that splat and channel. It is evaluated based on the direction \mathbf{d} extending from the camera to the splat center, as follows:

$$C(\mathbf{d}) = \sum_{i=1}^M L_i Y_i(\mathbf{d}), \quad (5)$$

where L_i represents the lighting coefficient corresponding to Y_i .

IV. METHOD

This section discusses the different steps of our proposed encoder, for which Figure 2 provides an overview. First, Section IV-A introduces a preliminary metric that is used throughout POTR. Next, we focus on splat removal, the first step of our encoder, with Section IV-B detailing how our proposed method can efficiently and accurately calculate the effect of a splat’s removal. This information is used in Section IV-C as the basis for our proposed splat-removal method. After pruning, we use a novel spherical harmonics energy compaction method to reduce the lighting coefficients’ entropy in Section IV-D. To complete our codec, Section IV-E discusses tangential topics such as quantization, serialization, entropy compression, and how these are all combined. Finally, Section IV-F discusses how our codec can be adapted to incorporate fine-tuning.

A. Splat importance

POTR utilizes lossy compression, during which a splat may be removed or its properties altered. The impact of modifying or removing a splat on the quality of the model varies heavily based on the splat in question. To help upcoming lossy steps gauge this impact, we define the importance $I_k(\mathbf{s})$ of the k -th splat to a camera \mathbf{s} as the fraction of the camera’s synthesized image that originates from the k -th splat, i.e.

$$I_k(\mathbf{s}) = \frac{1}{P} \sum_{\mathbf{x}} T_{ik} \alpha_{ik} \quad (6)$$

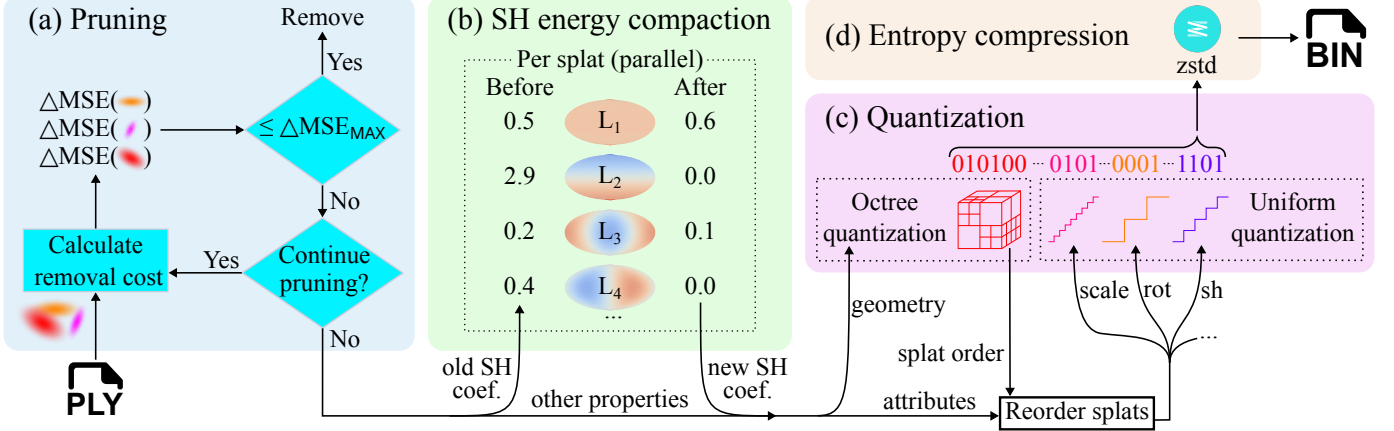


Fig. 2: Simplified overview of POTR. (a) Splats are removed across multiple pruning iterations based on the change in the model’s mean square error (MSE) upon their removal. (b) Spherical harmonic coefficients are energy compacted, yielding a new set of lighting coefficients with a lower entropy. (c) Splat geometry is quantized and serialized using an octree, then attributes are uniformly quantized and serialized using the spatial order implied by the depth-first traversal of the octree. (d) The serialized data is entropy compressed using zstd, resulting in the final compressed bitstream.

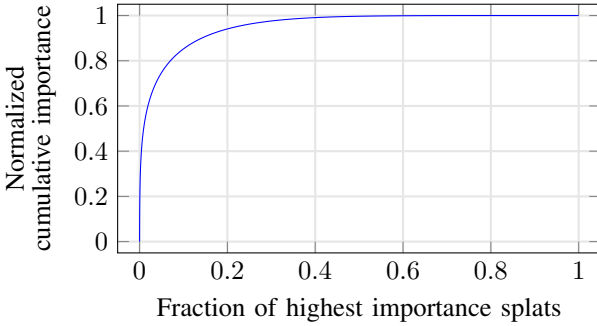


Fig. 3: Normalized cumulative importance of the highest importance splats in the Truck model of the initial 3DGS implementation [11]. The cumulative importance is the sum of the per-splat importances I_k for a given subset of splats.

where P is the number of pixels and i_k is the rank of the k -th splat in the alpha-compositing process for the pixel \mathbf{x} . The importance of a splat can be generalized to account for the entire scene, encompassing all N cameras, as follows:

$$I_k = \frac{1}{N} \sum_s I_k(s). \quad (7)$$

Figure 3 shows that a small fraction of splats draws the vast majority of a scene, highlighting the immense potential of selective loss introduction in a compression context.

B. Effect of a splat’s removal

Removing splats is a common way to reduce the final file size. To help determine if a splat is to be kept or removed, we desire a score that describes the impact of a splat’s removal on the quality of the scene. Other post-training compression methods rely solely on heuristics to set this score, for example, using a splat’s size or importance I_k . However, these approaches tend to be sub-optimal as they overlook

crucial factors such as color information and the intricate geometry of the model. For instance, the effect of removing a red splat varies depending on the splats that lie behind it. If this is another red splat, the change in the rendered image will be relatively minor. Conversely, the visual difference will be much more pronounced if a blue splat lies behind the red splat. Metrics such as a splat’s importance I_k fail to capture such nuances.

To address this limitation, we propose to modify the original rasterizer’s forward rendering pass to accurately evaluate the effect of removing a splat, for all splats simultaneously. Our proposed modification utilizes readily available data, specifically the opacities of the contributing splats for each pixel and the partial colors $\{\mathbf{P}_i\}$. The latter is a pixel’s color after i splats have been considered in the alpha compositing process and can be expressed as

$$\mathbf{P}_i = \sum_{k=0}^{i-1} T_k \alpha_k \mathbf{c}_k. \quad (8)$$

Removing the k -th splat with rank i_k in the alpha-compositing process of a given pixel renormalizes the transmittance of all subsequent splats by a factor of $\frac{1}{1-\alpha_{i_k}}$. Using this observation together with Equations (4) and (8), we derive a compact expression for the pruning difference $\mathbf{PD}_k(\mathbf{x})$, which quantifies the change in a pixel’s color resulting from the removal of the k -th splat:

$$\begin{aligned} \mathbf{PD}_k(\mathbf{x}) &= \tilde{\mathbf{c}}_k(\mathbf{x}) - \mathbf{c}(\mathbf{x}) \\ &= \left(\sum_{j=0}^{i_k-1} T_j \alpha_j \mathbf{c}_j + \frac{1}{1-\alpha_{i_k}} \sum_{j=i_k+1}^{K-1} T_j \alpha_j \mathbf{c}_j \right) - \mathbf{c}(\mathbf{x}) \\ &= (\mathbf{P}_{i_k} + \frac{1}{1-\alpha_{i_k}} (\mathbf{P}_K - \mathbf{P}_{i_k+1})) - \mathbf{P}_K \\ &= \mathbf{P}_{i_k} - \frac{1}{1-\alpha_{i_k}} \mathbf{P}_{i_k+1} + \frac{\alpha_{i_k}}{1-\alpha_{i_k}} \mathbf{P}_K, \end{aligned} \quad (9)$$

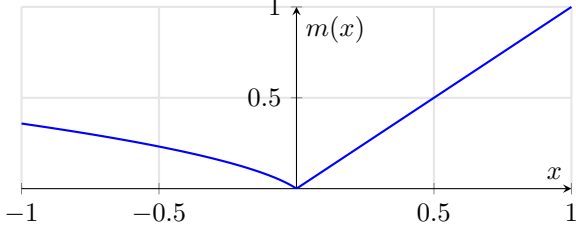


Fig. 4: The mapping function $m(x)$ for $a = 10$.

where $\mathbf{c}(\mathbf{x})$ and $\tilde{\mathbf{c}}_k(\mathbf{x})$ denote a pixel's color before and after removing the k -th splat, respectively.

The pruning difference is crucial for determining the impact of each splat's removal on an objective quality metric. In this initial work, the squared error is used due to its simplicity and relation to the PSNR. The difference in squared error, per pixel and color channel, as a result of removing the k -th splat is given by

$$\begin{aligned}\Delta \mathbf{SE}_k(\mathbf{x}) &= (\tilde{\mathbf{c}}_k(\mathbf{x}) - \mathbf{c}_t(\mathbf{x}))^2 - (\mathbf{c}(\mathbf{x}) - \mathbf{c}_t(\mathbf{x}))^2 \\ &= (\tilde{\mathbf{c}}_k(\mathbf{x}) - \mathbf{c}(\mathbf{x}))(\tilde{\mathbf{c}}_k(\mathbf{x}) + \mathbf{c}(\mathbf{x}) - 2\mathbf{c}_t(\mathbf{x})) \\ &= (\mathbf{PD}_k(\mathbf{x}))^2 + 2 \mathbf{PD}_k(\mathbf{x}) (\mathbf{c}(\mathbf{x}) - \mathbf{c}_t(\mathbf{x})),\end{aligned}\quad (10)$$

where $\mathbf{c}_t(\mathbf{x})$ is a fixed reference target color, defined as the initial synthesized color of the uncompressed model¹ such that initially $\mathbf{c}_t(\mathbf{x}) = \mathbf{c}(\mathbf{x})$. In Section IV-C, we will recompute $\Delta \mathbf{SE}_k(\mathbf{x})$ after removing splats, which changes $\mathbf{c}(\mathbf{x})$, $\tilde{\mathbf{c}}_k(\mathbf{x})$, and consequently $\mathbf{PD}_k(\mathbf{x})$, but not $\mathbf{c}_t(\mathbf{x})$. By averaging the change in squared error across all N cameras, P pixels, and 3 color channels, we arrive at the overall effect of the k -th splat's removal on the mean squared error of the model:

$$\Delta \mathbf{MSE}_k = \frac{1}{N} \sum_s \frac{1}{P} \sum_{\mathbf{x}} \frac{1}{3} \Delta \mathbf{SE}_k(\mathbf{x}) \cdot 1. \quad (11)$$

Finally, it should be noted that our CUDA implementation of the above method is deliberately designed to be interoperable with the standard forward-backward render pass used during training. The forward pass comes at no extra cost if our altered render pass is already executed to calculate the splats' removal effects. Future work could explore how our implementation can be properly integrated into the training process.

C. Iterative pruning

The *pruning controller* manages the removal of splats based on the $\Delta \mathbf{MSE}_k$ values. It operates under the assumption that the cumulative effect of removing a group of splats \mathcal{S} is approximately the sum of the individual effects, i.e.

$$\Delta \mathbf{MSE}_{\mathcal{S}} \approx \sum_{k \in \mathcal{S}} \Delta \mathbf{MSE}_k. \quad (12)$$

This assumption, which we call the *pruning approximation*, tends to grossly underestimate $\Delta \mathbf{MSE}_{\mathcal{S}}$ when removing too

¹Another valid choice for the target color $\mathbf{c}_t(\mathbf{x})$ is the ground truth color. However, our limited experiments indicate that its usage does not necessarily yield better results. Furthermore, since this work focuses on *post*-training compression, ground truth images are not always available.

many splats at once. To counteract this limitation, we propose an iterative approach with multiple pruning iterations where all $\Delta \mathbf{MSE}_k$ values are recalculated in between pruning iterations. In each iteration, the set of splats \mathcal{S} to be removed is constructed by iteratively adding splats to an empty set until the pruning budget $\mathcal{B}_{\text{prune}}$ is reached. We use the importance of a splat I_k as a simple estimate for the splat's ability to distort the pruning approximation, defining the pruning budget to be reached when

$$\mathcal{B}_{\text{prune}} \leq \sum_{k \in \mathcal{S}} I_k. \quad (13)$$

The pruning controller aims to remove all splats where $\Delta \mathbf{MSE}_k < \Delta \mathbf{MSE}_{\text{MAX}}$, and adjusts its pruning budget accordingly every iteration to achieve this:

$$\mathcal{B}_{\text{prune}} = \frac{1}{\# \text{ remaining iterations}} \sum_{k \in \{j \mid \Delta \mathbf{MSE}_j < \Delta \mathbf{MSE}_{\text{MAX}}\}} I_k. \quad (14)$$

The pruning controller adds splats to \mathcal{S} in ascending order of their $m(\frac{\Delta \mathbf{MSE}_k}{\Delta \mathbf{MSE}_{\text{MAX}}})$ value where

$$m(x) = \begin{cases} x & x \geq 0 \\ \frac{1}{a}(\sqrt{1 - 2a \cdot x} - 1) & x < 0 \end{cases} \quad (15)$$

is a mapping function (see Figure 4). This function is designed to prioritize the removal of splats with a small or negative $\Delta \mathbf{MSE}_k$ value, with the parameter a controlling the balance between these two objectives. By prioritizing splats with small $\Delta \mathbf{MSE}_k$, often more than 50% of the splats can be removed in just one iteration, accelerating subsequent pruning. On the other hand, focusing on splats with a negative $\Delta \mathbf{MSE}_k$ value helps minimize quality loss during the pruning process.

D. Spherical harmonics energy compaction

Spherical harmonics, and their coefficients, define a splat's color for every direction. However, in practice, most splats are sampled only from a small subset of directions. This phenomenon arises for various reasons, including occlusion between splats, and the observer's restricted range of motion. This section's key idea is to use this phenomenon to find alternate, easier-to-compress, lighting coefficients that retain the color within the sampled subset while being agnostic to color changes outside the sampled subset. Since color changes only occur for unsampled directions, the model's overall quality is unaffected.

To find an alternate set of lighting coefficients, we first observe that Equation (5) holds for all N training cameras resulting in N equations per splat that can be rewritten as follows:

$$\begin{pmatrix} C(\mathbf{d}_1) \\ C(\mathbf{d}_2) \\ \vdots \\ C(\mathbf{d}_N) \end{pmatrix} = \begin{pmatrix} Y_1(\mathbf{d}_1) & Y_2(\mathbf{d}_1) & \cdots & Y_M(\mathbf{d}_1) \\ Y_1(\mathbf{d}_2) & Y_2(\mathbf{d}_2) & \cdots & Y_M(\mathbf{d}_2) \\ \vdots & \vdots & \ddots & \vdots \\ Y_1(\mathbf{d}_N) & Y_2(\mathbf{d}_N) & \cdots & Y_M(\mathbf{d}_N) \end{pmatrix} \times \begin{pmatrix} L_1 \\ L_2 \\ \vdots \\ L_M \end{pmatrix} \quad (16)$$

We propose to use conventional energy compaction to find a new \mathbf{L} , denoted as \mathbf{L}' , located on the RD Pareto front by

using all N training cameras. This work uses ridge regression to define the optimal trade-off:

$$\mathbf{L}' = \arg \min_{\mathbf{x} \in \mathbb{R}^{M \times 1}} (\|\mathbf{Y}\mathbf{x} - \mathbf{C}\|_2^2 + \|\mathbf{\Gamma}\mathbf{x}\|_2^2) \quad (17)$$

where $\|\cdot\|_2$ is the Euclidean norm of a vector, and $\mathbf{\Gamma}$ denotes the Tikhonov matrix which defines how the lighting coefficients are regularized. The Tikhonov matrix is chosen as follows:

$$\mathbf{\Gamma} = \sqrt{\lambda} \begin{pmatrix} 0 & \mathbf{0}_{1 \times M-1} \\ \mathbf{0}_{M-1 \times 1} & \mathbf{I}_{M-1 \times M-1} \end{pmatrix} \quad (18)$$

where λ is the regularization coefficient and \mathbf{I} denotes the identity matrix. The top-left element is zero as we do not wish to regularize the DC lighting coefficient. The benefit of ridge regression, and the reason it was chosen for this work as opposed to other regularization techniques, is its closed-form solution:

$$\mathbf{L}' = (\mathbf{Y}^T \mathbf{Y} + \mathbf{\Gamma}^T \mathbf{\Gamma})^{-1} \mathbf{Y}^T \mathbf{C} \quad (19)$$

A closed-form solution is essential as \mathbf{L}' has to be calculated for each splat, with models having hundreds of thousands to millions of splats.

With the core idea in place, we propose four additional modifications to improve RD performance further:

1) *Importance*: Equation (17) punishes each deviation from \mathbf{C} equally, regardless of the importance of the splat to the camera. However, we expect a deviation in a splat's color (as perceived by a given camera) to affect the quality of a model approximately in accordance with the importance of that splat to that camera. We can take this into account by doing the following substitutions in Equation (17) (and Equation (19)):

$$\mathbf{C} \leftarrow \mathbf{C} \odot_{\text{col}} (I_k(\mathbf{s}_1), \dots, I_k(\mathbf{s}_N))^T \quad (20)$$

$$\mathbf{Y} \leftarrow \mathbf{Y} \odot_{\text{col}} (I_k(\mathbf{s}_1), \dots, I_k(\mathbf{s}_N))^T \quad (21)$$

where \odot_{col} represents a column element-wise multiplication.

2) *Color model*: RGB lighting coefficients correlate highly across color channels. By switching to a luminance-chrominance color model, we decorrelate the color channels and as a result, reduce the total energy. Additionally, chrominance channels can be more aggressively regularized, as human vision is less sensitive to chrominance changes. For this work, we use the YCoCg color model and regularize the chrominance channels thrice as hard by setting $\lambda = \lambda_Y = \frac{1}{3}\lambda_{Co} = \frac{1}{3}\lambda_{Cg}$. Surprisingly, to the best of our knowledge, this is the first post-training 3DGS compression work to use a non-RGB color model.

3) *Sparsity*: Due to the limited set of sampled directions, column vectors of \mathbf{Y} often exhibit quasi-parallelism among themselves, suggesting that lighting coefficients can be sparsified. Unfortunately, ridge regression spreads energy across parallel column vectors, leading to a non-sparse and under-regularization solution. We address this by zeroing out the i -th column of \mathbf{Y} , which leads to $L'_i = 0$, if a preceding column is 'sufficiently parallel' to it. Two column vectors are said to be sufficiently parallel if the absolute value of their cosine similarity is larger than some threshold α .

4) *Two-pass regularization*: Ridge regression forces a large number of AC lighting coefficients to be *almost* zero such that these lighting coefficients will be quantized to zero in Section IV-E. To reduce the quantization loss and to present ridge regression with a more true representation of its flexibility, a two-pass regularization system is used. The first pass identifies all almost zero AC coefficients and subsequently forces them to zero. The second pass finds the optimal values for the remaining non-zero lighting coefficients.

In summary, we demonstrate that a splat's color for all N training cameras can be expressed as one linear system of lighting coefficients. We then propose to use ridge regression to find a new set of lighting coefficients with a lower entropy. Finally, we improve upon this basic energy compaction method through importance weighting, a luminance-chrominance model, the removal of parallel column vectors, and a two-pass regularization system.

E. Codec

We use the proposed pruning and spherical harmonics energy compaction methods to create a codec (see Figure 2). The encoder first removes redundant splats before spherical harmonics energy compaction reduces the entropy of the remaining splats' lighting coefficients. Subsequently, the geometry and attributes are quantized and serialized contiguously into a bitstream, iterating over all splats before serializing the next property. Finally, the bitstream is compressed using zstd², an out-of-the-box lossless compression algorithm, yielding the final compressed bitstream. The decoder follows the opposite process by decompressing using zstd, deserializing, and dequantizing the bitstream, in that order.

Quantization is performed using multiple strategies. The splat attributes (scale, rotation, opacity, and SH coef.) are uniformly quantized and dequantized using the transformations

$$\hat{x} = \left\lfloor \frac{1}{2} + x \cdot \text{SF} \right\rfloor \quad \text{and} \quad \tilde{x} = \frac{\hat{x}}{\text{SF}}, \quad (22)$$

where SF is the scale factor, a hyperparameter tailored to each attribute. Unlike attribute quantization, the geometry of the splats is quantized using an octree structure. Each splat's position μ is quantized to the center of an octree leaf $\hat{\mu}$. The octree is constructed by repeatedly splitting leaves containing multiple splats or failing to meet the precision criterion

$$\|\mu - \hat{\mu}\|_2 < \max \left(\gamma, \beta \cdot \min_s \|\mu - \mu_s\|_2 \right), \quad (23)$$

where $\|\cdot\|_2$ denotes the Euclidean distance, μ_s is the position of the eye of camera s , and β and γ are hyperparameters. This criterion leverages the observation that positional changes of distant splats have minimal impact on their screen-space positions. We serialize the octree using a depth-first traversal. Upon visiting a node for the first time, we append its occupancy to the bitstream. The occupancy of an octree's node is a single byte in which each bit corresponds to one of the eight octants and indicates whether that octant contains a child node.

²<https://github.com/facebook/zstd>

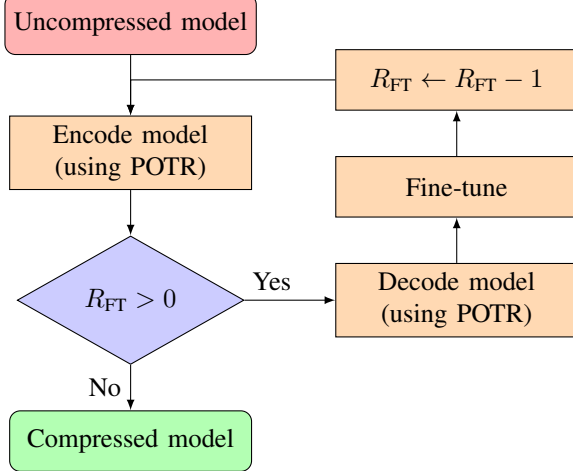


Fig. 5: Schematic representation of the POTR-FT encoder. R_{FT} denotes the remaining number of fine-tuning cycles.

Our codec also employs some additional optimizations. For instance, DC lighting coefficients are differentially encoded, the real quaternion component of the rotation is omitted, and opacity reconstruction values are shifted off-center during dequantization by using $\tilde{x} = \frac{\hat{x}+0.25}{SF}$ (see Equation (22)). We also note that the order of the steps shown in Figure 2 is flexible. For example, spherical harmonics energy compaction can be applied earlier, e.g., after half of the pruning iterations, to allow the remaining iterations to account for the changes introduced by energy compaction.

F. Fine-tuning

To enable a fair comparison of our proposed codec with others that incorporate fine-tuning, we introduce a variant of POTR, called POTR-FT, which includes a fine-tuning mechanism. Since fine-tuning is not the focus of this work, we deliberately keep POTR-FT’s design simple. Specifically, its encoder employs the original (fine-tuneless) encoder and decoder as an internal black-box component, performing R_{FT} cycles of decode \rightarrow fine-tune \rightarrow encode, following the initial encoding. The fine-tuning step trains the model using the original 3DGS training routine. The encoder design of POTR-FT is depicted in Figure 5.

V. EXPERIMENTS AND DISCUSSION

We present and discuss our codec’s performance using the methodology laid out by 3DGS.zip [73], a 3DGS compression survey focusing on low distortion. If 3DGS.zip’s methodology provides no guidance, we follow the initial 3DGS implementation’s [11] approach where possible.

The remainder of this section is structured as follows. First, we discuss our experimental settings in Section V-A. Afterward, we present POTR’s quantitative and qualitative results in Section V-B. In Section V-C and Section V-D we take a closer look at our proposed pruning and spherical harmonics energy compaction approach respectively. In Section V-E we present two ablation studies, and in Section V-F we discuss our codec’s speed.

A. Experimental settings

1) *Datasets*: We evaluate our codec across four datasets: three COLMAP [74] datasets (Mip-NeRF 360 [13], Deep Blending [75], and Tanks And Temples [76]) and one Blender dataset (NeRF-Synthetic [10]). For the COLMAP datasets, every 8th image is designated for testing, while the Blender dataset comes with a predefined train-test split. The additional Mip-NeRF 360 scenes (*flowers* and *treehill*) are included and outdoor scenes (*bicycle*, *flowers*, *stump*, *treehill*, *garden*) are downsampled 4x while indoor scenes (*counter*, *kitchen*, *room*, *bonsai*) are downsampled 2x.

2) *Models*: As POTR is a *post*-training compression codec, a trained model is required to use our proposed codec. We use the models published alongside the initial 3DGS implementation³ where possible, however, NeRF-Synthetic models are absent from this collection. We train these models ourselves using the configuration provided by 3DGS’s initial implementation.

3) *Hyperparameters*: All hyperparameters are governed by a single quality parameter q as specified by Table II. We set q to 0.5 in spirit, but to match the results of other works, we alter it slightly per dataset such that POTR’s objective quality slightly exceeds those of other compression works. In comparison, MesonGS [46] sets their hyperparameters on a per-scene basis. This yields further non-negligible RD gains but is currently done manually or at great computational cost. Finally, for POTR-FT, we use two fine-tuning cycles ($R_{FT} = 2$) of 500 training iterations each. To ensure fairness, comparisons to other fine-tuning methods match the total number of training iterations.

4) *Metrics*: Our evaluation focuses predominately on RD performance, with visual quality being objectively assessed using PSNR, SSIM [77], and LPIPS [78]. We also report inference time, though it is inherently hardware-dependent. For a hardware-agnostic indicator of computational cost, we additionally consider the number of splats.

B. Codec results

Table I and Figure 6 respectively present the quantitative and qualitative performance of POTR(-FT). POTR achieves compression ratios of 20–45x while retaining the models’ quality, surpassing all other post-training codecs. This highlights that no fine-tuning is required to achieve strong RD performance. Using fine-tuning, POTR-FT further improves POTR’s already superior RD performance, reducing storage requirements by 35–50% for the Deep Blending dataset, as shown in Figure 7. Notably, the same figure shows that POTR(-FT) surpasses the baseline’s quality at sufficiently high q , even without fine-tuning.

POTR(-FT)’s strong RD performance primarily results from our superior pruning method as our compressed models typically use more bytes per splat than other post-training methods. We suspect that the latter results from our comparatively simple quantization, serialization, and entropy compression

³<https://repo-sam.inria.fr/fungraph/3d-gaussian-splatting/datasets/pretrained/models.zip>

Ground-truth		Size		# of splats		Size		# of splats		Size		# of splats		Size		# of splats	
Baseline																	
No fine-tuning	POTR (ours)	12.5 MB	822 k			40.7 MB	2.36 M			13.7 MB	635 k			4.00 MB	192 k		
MesonGS	MesonGS	22.5 MB	1.52 M			57.6 MB	4.20 M			29.0 MB	2.04 M			4.42 MB	274 k		
Fine-tuning	POTR-FT (ours)	10.2 MB	691 k			31.7 MB	1.94 M			9.64 MB	466 k			3.22 MB	161 k		
MesonGS-FT	MesonGS-FT	22.5 MB	1.52 M			57.6 MB	4.20 M			29.0 MB	2.04 M			4.42 MB	274 k		
C3DGS	C3DGS	22.4 MB	2.05 M			49.1 MB	5.32 M			22.8 MB	2.28 M			4.99 MB	333 k		

Fig. 6: Qualitative comparison of our proposed codec (POTR and POTR-FT) with the baseline (Kerbl et al. [11]) and the state-of-the-art in post-training 3DGS compression (MesonGS, MesonGS-FT [46], and C3DGS [47]). One scene per discussed dataset is considered, namely (from left to right): Truck (Tanks And Temples), Garden (Mip-NeRF 360), Playroom (Deep Blending), and Lego (NeRF-Synthetic). Every model is annotated with its size and the number of splats.

Method	Lossless Format	FT	Tanks And Temples				Mip-NeRF 360				Deep Blending				NeRF-Synthetic							
			PSNR↑	SSIM↑	LPIPS↓	Size MB ↓	PSNR↑	SSIM↑	LPIPS↓	Size MB ↓	PSNR↑	SSIM↑	LPIPS↓	Size MB ↓	PSNR↑	SSIM↑	LPIPS↓	Size MB ↓				
Baseline [11]	-	-	23.36	.838	.186	442	1,784	27.47	.821	.206	834	3,362	29.43	.898	.246	738	2,976	33.79	.970	.030	71.8	289
MesonGS [46]	npz	No	22.84	.820	.211	17.3	1,163	26.22	.785	.249	29.7	2,147	28.70	.890	.271	29.0	2,023	32.49	.962	.039	3.52	210
MesonGS-FT [46]	npz	Yes	23.16	.832	.200	17.3	1,163	27.03	.805	.231	29.7	2,147	29.54	.901	.255	29.0	2,023	33.25	.966	.035	3.51	210
C3DGS [47]	npz	Yes	23.13	.834	.195	18.3	1,483	27.16	.811	.226	30.4	2,973	29.35	.901	.256	26.7	2,613	33.31	.968	.033	3.99	270
LightGaussian [31]	npz	Yes	22.86	.817	.215	29.1	607	26.75	.805	.244	54.5	1,143	29.16	.894	.261	47.9	1,012	31.33	.956	.047	4.92	99
POTR (ours)	npz	No	23.27	.834	.191	12.8	690	27.08	.806	.226	29.3	1,500	29.31	.897	.253	18.6	785	33.34	.968	.032	3.94	154
POTR-FT (ours)	npz	Yes	23.34	.837	.189	10.6	594	27.20	.808	.223	24.1	1,285	29.44	.902	.250	13.2	585	33.37	.968	.032	3.12	126
	zstd																					

TABLE I: Quantitative comparison of our proposed codec with the baseline (uncompressed starting scene) and other compression methods. The first, second, and third best compression results are highlighted for each metric across different datasets. The 'FT' column indicates whether a method utilizes fine-tuning. All fine-tuning methods use 1,000 training iterations. The 'Lossless Format' column indicates the lossless compression method used: NumPy's (npz) or Meta's Zstandard (zstd).

Parameter	Value	Parameter	Value
λ	10^{-q}	SF _{SH}	$1 + 100q$
α	sigmoid($3q$)	SF _{opacity}	$1 + 200q$
$\Delta \text{MSE}_{\text{MAX}}$	$10^{-8.8-2q}$	SF _{rotation}	$1 + 400q$
β	$1.4 \cdot 10^{-4} \cdot q$	SF _{scale}	$1 + 4000q$
γ	$5.0 \cdot 10^{-3-5q}$	# pruning iterations	48

TABLE II: Hyperparameters as functions of $q \in [0, 1]$.

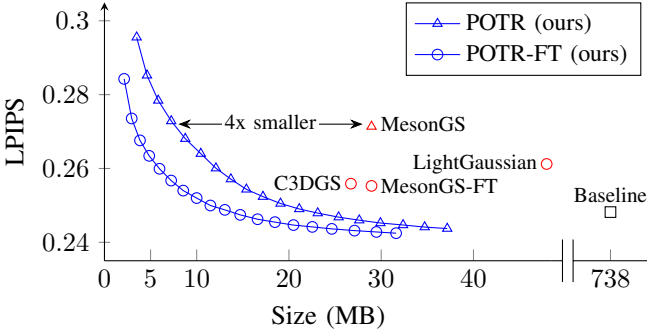


Fig. 7: RD performance comparison of various post-training methods on the Deep Blending dataset. Circle markers (○) indicate methods that utilize fine-tuning, while triangle markers (△) denote methods without fine-tuning.

scheme. We believe future works could combine our ideas with existing literature to further improve RD performance.

C. Pruning

Existing pruning methods are typically just as capable as POTR at removing trivial and low-importance splats. It is primarily after these splats are removed that our pruning method starts to meaningfully outperform other methods. As a result, our method keeps becoming comparatively better than other methods as more and more distortion is tolerated. To illustrate this, Figure 8 shows the relation between the PSNR and the fraction of splats removed for various pruning methods. Here, all methods remove the first 40% of splats quasi-losslessly, but afterward, performances start to diverge significantly. For a PSNR of 27, POTR requires 29% fewer splats than MesonGS and LightGaussian, but for a PSNR of

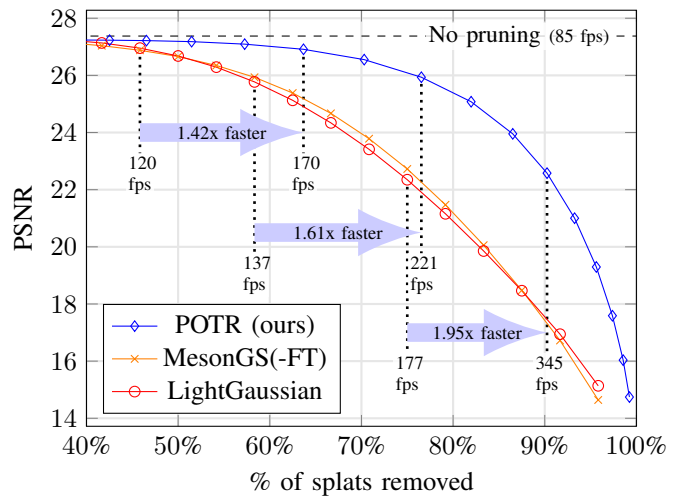


Fig. 8: Quantitative comparison of post-training pruning methods for the Garden model. Frame rate values represent rendering at 1080p on an RTX 2080 Ti. LightGaussian and MesonGS inference speeds are shown as one as they are quasi-equal.

22, this has more than doubled to POTR requiring 64% fewer splats.

Figure 8 also shows that our pruning method leads to markedly faster inference times. While this is primarily due to POTR simply removing more splats, there is a less obvious secondary phenomenon at play as models created by POTR can have far more splats, while still achieving the same inference speed as other methods. For example, Figure 8 shows that LightGaussian and MesonGS reach 177 fps after removing 75% of splats while POTR only has to remove a little over 65% of splats to achieve the same inference speed. Upon closer inspection, we find that despite our model having more splats, it has fewer Gaussian instances during rendering for common camera poses. We suspect that this is due to our method removing more splats that are more frequently in view, but further research is required to verify this.

Beyond RD performance and inference speed, various other topics benefit from having a better removal order. Examples

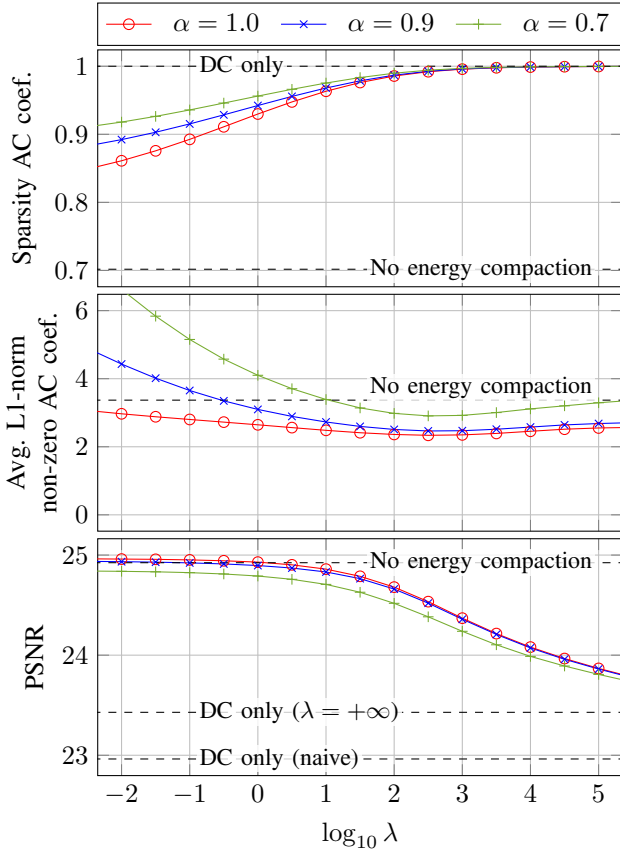


Fig. 9: Effect of λ and α on the magnitude and sparsity of the AC lighting coefficients and PSNR for the Truck model (post-pruning and post-quantization). 'Naive' refers to setting all AC lighting coefficients to zero without recomputing the DC lighting coefficients.

include level-of-detail rendering and progressive loading more broadly. Future works could look at how our proposed pruning method can be adapted to these purposes.

D. Spherical harmonics energy compaction

To better understand the effectiveness of spherical harmonics energy compaction at lowering the entropy of the AC lighting coefficients, we analyze how λ and α influence the magnitude and sparsity of the AC lighting coefficients and quality of the model. Figure 9 shows that the sparsity increases far more quickly than the PSNR decreases upon applying harsher regularization. This is despite the magnitude of non-zero AC lighting coefficients remaining relatively constant, indicating that by carefully choosing λ and α , the entropy of the AC lighting coefficients can be dramatically reduced while minimally impacting the PSNR. For example in Figure 9 for $\lambda = 10^{1.1}$ and $\alpha = 0.9$, the number of non-zero AC coefficients decreases 10-fold. Despite eliminating 90% of non-zero AC coefficients, the PSNR is minorly impacted, going from 24.97 to 24.82. Further removing the remaining 10% of AC coefficients would cause an 11-fold larger increase in the MSE, highlighting our method's effectiveness in identifying

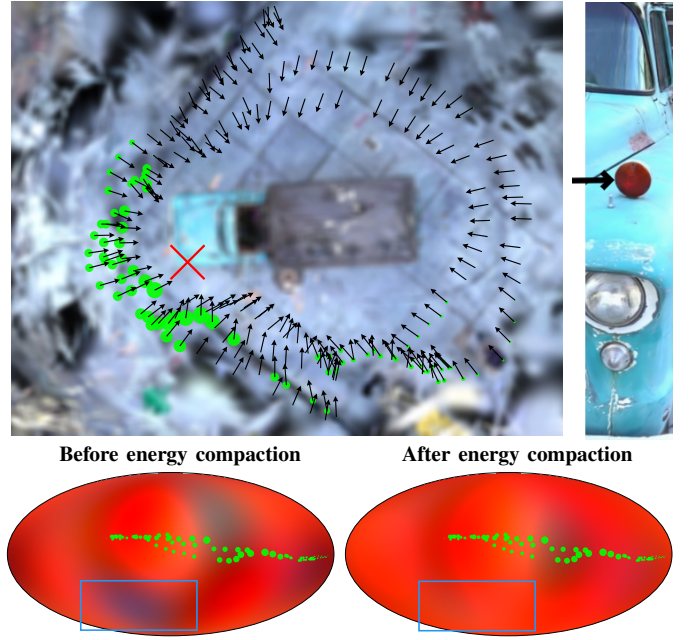


Fig. 10: A blurred, top-down view of the Truck model shows a red cross marking a splat from the truck's red reflector. Each training camera s is represented by a black arrow, indicating its viewing direction, and a green dot whose size is proportional to $I_k(s)$. On the bottom, Mollweide projections depict the splat's view-dependent color before and after energy compaction, where every green dot again corresponds with a camera. Energy compaction results in a lower energy alias that removes a hallucinated blue color (highlighted by a blue rectangle) from an unsampled viewing area.

each lighting coefficient's importance to the quality of the model.

To practically illustrate the impact of energy compaction, we examine a single splat in Figure 10. Here, training cameras with high importance preserve their directions' colors while other directions' colors change in favor of a low-energy alias. As low-energy aliases typically correspond to 'simpler' solutions, we indirectly follow Occam's razor which often leads to more sensible generalizations for unseen viewpoints. Originally the splat in the red reflector became blue when looked at from below, but with the simpler alias, the red reflector stays red. More broadly, we suspect low-energy aliases to be the driving force behind the PSNR increasing slightly, from 24.97 to 24.97 under minimal regularization in Figure 9. Notably, this increase in PSNR is achieved without using any ground-truth images.

A key advantage of our energy compaction approach is its adaptability to model- and scene-specific characteristics. For example, the geometry of the scene and the camera trajectory are clearly reflected in the sparsity of the spherical harmonics bases. For the Truck model, splats are primarily observed from the side. Low-energy solutions prefer spherical harmonics bases that change significantly across samples as this leads to smaller coefficients. As a result, the energy compacted Truck model has three times fewer non-zero L_2 than non-

	PSNR↑	SSIM↑	LPIPS↓	Size↓ MB	# Splats↓ x1,000
3DGS baseline	25.46	.775	.210	1,521	6,132
Ours					
+ Serialization & Quantization	25.10	.760	.213	715.5	6,132
+ Entropy compression	25.10	.760	.213	189.3	6,132
+ Pruning	25.05	.755	.220	91.44	2,656
+ SH compaction	25.03	.754	.221	57.40	2,626
+ RGB → YCoCg	25.01	.753	.224	41.53	2,624
+ Fine-tuning	25.19	.758	.219	33.86	2,221

TABLE III: Ablation study for the different components of the POTR(-FT) encoder for the Bicycle model.

Splat property	Bytes per splat (%)		Compression factor
	Uncompressed	Compressed	
Position	12 (5.1%)	3.58 (23 %)	3.35x
Scale	12 (5.1%)	2.40 (16 %)	6.45x
Opacity	4 (1.7%)	0.72 (4.7 %)	5.59x
Rotation	16 (6.8%)	3.29 (22 %)	4.87x
DC SH coeffs.	12 (5.1%)	2.24 (15 %)	5.37x
AC SH coeffs.	180 (76%)	3.03 (20 %)	59.4x
Total	236 (100%)	15.3 (100%)	15.5x

TABLE IV: Effect of the post-pruning steps (no fine-tuning) on the size of the splat properties of the Bicycle model. A property’s compressed size is approximated through its ablation from the bitstream.

zero L_4 values as Y_2 remains relatively constant near the ‘equator’, while Y_4 changes substantially. Such observations imply further predictability of the lighting coefficients and are therefore useful for compression. POTR exploits these observations through its serialization order, but future works could exploit these observations more explicitly through, for example, a custom entropy model.

E. Ablation Study

Table III presents an ablation study that evaluates the incremental impact of the different components of our proposed codec. It reveals that quantization, combined with our serialization strategy and entropy compression, already compresses the Bicycle model 8x. Incorporating pruning further reduces the size by half, as more than half of the splats are removed. Spherical harmonics energy compaction provides an additional 37% size reduction while only modifying lighting coefficients and with virtually no quality loss. Similarly, switching from an RGB to a YCoCg color representation (including more harshly regularizing the chrominance channels) yields a further 28% reduction, again highlighting the importance of lighting coefficients to 3DGS compression.

Finally, fine-tuning consistently improves all metrics, reducing both distortion and the number of splats. This improvement arises because encoding and fine-tuning act in complementary ways: encoding is coarse, lossy, and approximate (e.g., pruning, quantization, and SH compaction), while fine-tuning corrects the resulting errors through small, precise, global adjustments. Iteratively alternating between encoding and fine-tuning can hence yield further gains, as each process creates additional rate-distortion improvement opportunities for the other. For instance, SH energy compaction recomputes all SH coefficients in a coarse, non-gradual manner based on

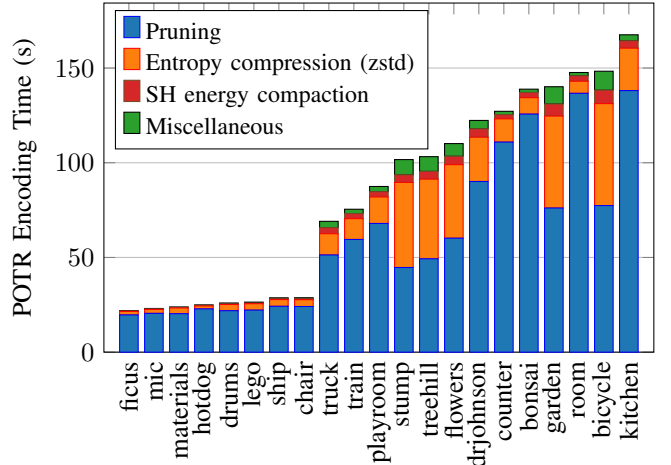


Fig. 11: POTR’s encoding time for various models. ‘Miscellaneous’ includes the remaining encoding operations, such as quantization and serialization.

approximate statistics. Fine-tuning then refines these coefficients holistically, applying small, accurate, and globally consistent corrections. In effect, fine-tuning validates the updates introduced by energy compaction, allowing the subsequent compaction step to be even more aggressive relative to the original SH coefficients.

To quantify the compression of lighting coefficients, we conduct a second ablation study, shown in Table IV, to evaluate the contribution of individual splat properties to the final compressed model size. We estimate a property’s contribution to the file size by measuring the reduction in the compressed model size when that property is removed from the bitstream⁴. Table IV reveals that the AC lighting coefficients are compressed by a factor of nearly 60x, whereas other properties achieve more modest compression factors of 3-6x. Consequently, AC lighting coefficients are no longer the primary contributors to the model size, with positional and rotational information each occupying a larger share.

F. Codec speed

POTR and POTR-FT make trade-offs between their speed and RD performance. For the results presented in Table I and Figure 6, RD performance is prioritized, however, POTR can still be fast. In this subsection we discuss the speed of our codec using an NVIDIA GeForce RTX 5090 and AMD Ryzen 9 9950X.

Decoding is extremely fast, with all but the largest models loading in one second or less. A linear model that fits the total decoding time in seconds y as a function of the number of splats post-pruning x with high accuracy is

$$y = 5.51 \times 10^{-7}x - 0.02 \quad (r > 0.999).$$

This corresponds to a decoding throughput of approximately 1.8 million splats per second, which is sufficient for most

⁴Zstd’s compressed bitstream can, strictly speaking, not be decomposed into distinct parts due to the holistic nature of lossless compression. However, this analysis only aims to provide an approximate understanding of each property’s contribution to the compressed file size.

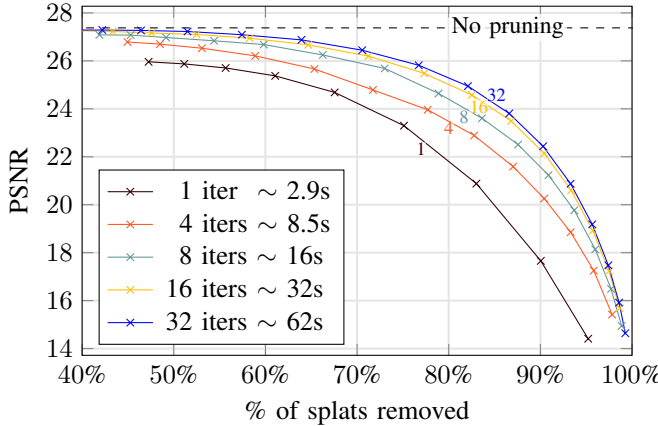


Fig. 12: The impact of limiting the number of pruning iterations on the Pareto front of POTR’s pruning method for the Garden model. Beyond 32 iterations (~ 62 seconds), the Pareto front still improves, but minorly.

practical use cases. The total decoding time is dominated by three operations: zstd decompression, octree deserialization, and attribute deserialization, which on average correspond to 10%, 62%, and 26% of total decode time respectively.

As shown in Figure 11, encoding is considerably slower, with POTR requiring between 20 and 170, seconds depending on the model. Because POTR-FT repeatedly performs encoding and its fine-tuning stage is comparatively fast, the total encoding time of POTR-FT is closely tied to that of POTR. Each of the R_{FT} fine-tuning cycles takes roughly 80% of the original encoding time, although this can be reduced substantially by integrating fine-tuning directly into the training loop. Figure 11 also breaks down the contribution of each encoding step to the overall encoding time, we discuss the three most important steps in order of their importance:

1) *Pruning*: Pruning is typically the most time-consuming step during encoding as every pruning iteration starts by recalculating all $\Delta M S E_j$ values by executing a modified forward pass per training view. Pruning time is therefore roughly linear in

- the number of training views,
- the time per modified forward pass, and
- the number of pruning iterations.

We expect that ideas from sparse scene reconstruction [79], [80] could be used to reduce the number of views rendered by an order of magnitude. Additionally, we expect that the time per modified forward pass can be further improved by carefully optimizing our modified forward pass. We leave improving and studying these ideas to future works and focus on the effect of reducing the number of pruning iterations. Figure 12 shows that the number of pruning iterations can be significantly reduced if a slightly lower RD performance is tolerated. Even using just one pruning iteration, our pruning performance is already on par with LightGaussian and MesonGS (also see Figure 8). Using only four pruning iterations, POTR outperforms all other pruning strategies. We use 48 pruning iterations (see Table II), which effectively guarantees that the

resulting RD performance is near-optimal.

2) *Entropy compression* : At the highest compression level, entropy compression (zstd) can be a major contributor to total runtime, especially for the larger models, since zstd encode time scales roughly linearly with the final splat count. Lowering the compression level can reduce this overhead to the point of being negligible. For instance, using zstd at level 4 instead of level 22 yields approximately a $100\times$ speedup, at the cost of only about a 10% increase in file size.

3) *Spherical harmonics energy compaction* : Our proposed spherical harmonics energy compaction method is embarrassingly parallel as each splat is processed independently. Furthermore, by using ridge regression, a closed-form solution is available that allows one of the 32 cores of our test machine to energy compact upto 14,000 splats per second. Using a sufficient number of threads thus makes the time spherical harmonics energy compaction takes inconsequential.

VI. CONCLUSION

This work introduced POTR, a post-training codec for 3D Gaussian Splatting that focuses on achieving strong rate-distortion performance without fine-tuning. We first identified that current post-training pruning methods rely heavily on heuristics which often leads to suboptimal splat removal decisions. To address this, we proposed an efficient method to precisely compute the impact of each splat’s removal on an objective quality metric. POTR leverages this knowledge to remove splats in a manner that far outperforms existing pruning methods, especially at higher distortion levels. Additionally, we proposed the first method to non-trivially reduce the entropy of 3DGS lighting coefficients without training. Our approach is fast, embarrassingly parallel, highly adaptable, and shown to generalize lighting information more sensibly. Combined with a simple quantization, serialization, and entropy compression scheme, these innovations allow POTR to significantly outperform existing methods in both rate-distortion performance and inference speed, despite not using fine-tuning. Moreover, we demonstrated that incorporating a simple fine-tuning scheme further enhances POTR’s rate-distortion performance and inference speed. We believe that our codec’s smaller file sizes and faster inference speeds could help make 3D Gaussian Splatting models more accessible, especially for on-demand and virtual reality applications.

REFERENCES

- [1] R.-S. Wang and Y. Wang, “Multiview video sequence analysis, compression, and virtual viewpoint synthesis,” *IEEE Transactions on Circuits and Systems for Video Technology*, vol. 10, no. 3, pp. 397–410, 2000.
- [2] J. Lu, S. Rogmans, G. Lafruit, and F. Catthoor, “Stream-centric stereo matching and view synthesis: A high-speed approach on gpus,” *IEEE Transactions on Circuits and Systems for Video Technology*, vol. 19, no. 11, pp. 1598–1611, 2009.
- [3] C. Song, S. Wang, J. Wei, and Y. Zhao, “Fewarnet: An efficient few-shot view synthesis network based on trend regularization,” *IEEE Transactions on Circuits and Systems for Video Technology*, vol. 34, no. 10, pp. 9264–9268, 2024.
- [4] K. Yamamoto, M. Kitahara, H. Kimata, T. Yendo, T. Fujii, M. Tanimoto, S. Shimizu, K. Kamikura, and Y. Yashima, “Multiview video coding using view interpolation and color correction,” *IEEE Transactions on Circuits and Systems for Video Technology*, vol. 17, no. 11, pp. 1436–1449, 2007.

[5] A. I. Purica, E. G. Mora, B. Pesquet-Popescu, M. Cagnazzo, and B. Ionescu, "Multiview plus depth video coding with temporal prediction view synthesis," *IEEE Transactions on Circuits and Systems for Video Technology*, vol. 26, no. 2, pp. 360–374, 2016.

[6] X. Tian, J. Shao, D. Ouyang, and H. T. Shen, "Uav-satellite view synthesis for cross-view geo-localization," *IEEE Transactions on Circuits and Systems for Video Technology*, vol. 32, no. 7, pp. 4804–4815, 2022.

[7] R. Verhach, T. Sikora, G. Van Wallendael, and P. Lambert, "Steered mixture-of-experts for light field images and video: Representation and coding," *IEEE Transactions on Multimedia*, vol. 22, no. 3, pp. 579–593, 2020.

[8] J. Artois, M. Courteaux, G. Wallendael, and P. Lambert, "Opendibr: Open real-time depth-image-based renderer of light field videos for vr," *Multimedia Tools and Applications*, vol. 83, pp. 25 797–25 815, 08 2023.

[9] M. Courteaux, H. Mareen, B. Ramlot, P. Lambert, and G. Van Wallendael, "Dimensionality reduction for the real-time light-field view synthesis of kernel-based models," *Electronics*, vol. 13, no. 20, 2024.

[10] B. Mildenhall, P. P. Srinivasan, M. Tancik, J. T. Barron, R. Ramamoorthi, and R. Ng, "Nerf: Representing scenes as neural radiance fields for view synthesis," in *ECCV*, 2020.

[11] B. Kerbl, G. Kopanas, T. Leimkühler, and G. Drettakis, "3d gaussian splatting for real-time radiance field rendering," *ACM Transactions on Graphics*, vol. 42, no. 4, July 2023.

[12] J. T. Barron, B. Mildenhall, M. Tancik, P. Hedman, R. Martin-Brualla, and P. P. Srinivasan, "Mip-nerf: A multiscale representation for anti-aliasing neural radiance fields," *ICCV*, 2021.

[13] J. T. Barron, B. Mildenhall, D. Verbin, P. P. Srinivasan, and P. Hedman, "Mip-nerf 360: Unbounded anti-aliased neural radiance fields," *CVPR*, 2022.

[14] —, "Zip-nerf: Anti-aliased grid-based neural radiance fields," *ICCV*, 2023.

[15] B. Kerbl, A. Meuleman, G. Kopanas, M. Wimmer, A. Lanvin, and G. Drettakis, "A hierarchical 3d gaussian representation for real-time rendering of very large datasets," *ACM Transactions on Graphics*, vol. 43, no. 4, July 2024.

[16] Y. Liu, H. Guan, C. Luo, L. Fan, J. Peng, and Z. Zhang, "Citygaussian: Real-time high-quality large-scale scene rendering with gaussians," 2024.

[17] G. Wu, T. Yi, J. Fang, L. Xie, X. Zhang, W. Wei, W. Liu, Q. Tian, and W. Xinggang, "4d gaussian splatting for real-time dynamic scene rendering," *arXiv preprint arXiv:2310.08528*, 2023.

[18] J. Luiten, G. Kopanas, B. Leibe, and D. Ramanan, "Dynamic 3d gaussians: Tracking by persistent dynamic view synthesis," in *3DV*, 2024.

[19] Y. Zhang, W. Jia, W. Niu, and M. Yin, "Gaussianspa: An "optimizing-sparsifying" simplification framework for compact and high-quality 3d gaussian splatting," in *Proceedings of the Computer Vision and Pattern Recognition Conference*, 2025, pp. 26 673–26 682.

[20] M. Wu and T. Tuytelaars, "Implicit gaussian splatting with efficient multi-level tri-plane representation," 2024.

[21] S. Lee, F. Shu, Y. Sanchez, T. Schierl, and C. Hellge, "Compression of 3d gaussian splatting with optimized feature planes and standard video codecs," *arXiv preprint arXiv:2501.03399*, 2025.

[22] W. Morgenstern, F. Barthel, A. Hilsmann, and P. Eisert, "Compact 3d scene representation via self-organizing gaussian grids," *arXiv preprint arXiv:2312.13299*, 2023.

[23] X. Liu, X. Wu, P. Zhang, S. Wang, Z. Li, and S. Kwong, "Compgs: Efficient 3d scene representation via compressed gaussian splatting," in *Proceedings of the 32nd ACM International Conference on Multimedia*, 2024, pp. 2936–2944.

[24] X. Liu, X. Wu, S. Wang, Z. Li, and S. Kwong, "Compgs++: Compressed gaussian splatting for static and dynamic scene representation," *arXiv preprint arXiv:2504.13022*, 2025.

[25] Y. Chen, Q. Wu, W. Lin, M. Harandi, and J. Cai, "Hac: Hash-grid assisted context for 3d gaussian splatting compression," in *European Conference on Computer Vision*, 2024.

[26] —, "Hac++: Towards 100x compression of 3d gaussian splatting," *arXiv preprint arXiv:2501.12255*, 2025.

[27] K. Navaneet, K. P. Meibodi, S. A. Koohpayegani, and H. Pirsiaavash, "Compact3d: Smaller and faster gaussian splatting with vector quantization," *arXiv preprint arXiv:2311.18159*, 2023.

[28] H. Wang, H. Zhu, T. He, R. Feng, J. Deng, J. Bian, and Z. Chen, "End-to-end rate-distortion optimized 3d gaussian representation," 2024.

[29] S. Girish, K. Gupta, and A. Shrivastava, "Eagles: Efficient accelerated 3d gaussians with lightweight encodings," 2024.

[30] T. Lu, M. Yu, L. Xu, Y. Xiangli, L. Wang, D. Lin, and B. Dai, "Scaffold-gs: Structured 3d gaussians for view-adaptive rendering," in *Proceedings of the IEEE/CVF Conference on Computer Vision and Pattern Recognition*, 2024, pp. 20 654–20 664.

[31] J. C. Lee, D. Rho, X. Sun, J. H. Ko, and E. Park, "Compact 3d gaussian representation for radiance field," in *Proceedings of the IEEE/CVF Conference on Computer Vision and Pattern Recognition (CVPR)*, 2024, pp. 21 719–21 728.

[32] X. Sun, J. C. Lee, D. Rho, J. H. Ko, U. Ali, and E. Park, "F-3dgs: Factorized coordinates and representations for 3d gaussian splatting," *arXiv preprint arXiv:2405.17083*, 2024.

[33] P. Papantonakis, G. Kopanas, B. Kerbl, A. Lanvin, and G. Drettakis, "Reducing the memory footprint of 3d gaussian splatting," *Proceedings of the ACM on Computer Graphics and Interactive Techniques*, vol. 7, no. 1, May 2024.

[34] Y. Wang, Z. Li, L. Guo, W. Yang, A. Kot, and B. Wen, "Contextgs: Compact 3d gaussian splatting with anchor level context model," *Advances in neural information processing systems*, vol. 37, pp. 51 532–51 551, 2024.

[35] S. Shin, J. Park, and S. Cho, "Locality-aware gaussian compression for fast and high-quality rendering," *arXiv preprint arXiv:2501.05757*, 2025.

[36] J. Cao, V. Goel, C. Wang, A. Kag, J. Hu, S. Korolev, C. Jiang, S. Tulyakov, and J. Ren, "Lightweight predictive 3d gaussian splats," *arXiv preprint arXiv:2406.19434*, 2024.

[37] G. Fang and B. Wang, "Mini-splatting: Representing scenes with a constrained number of gaussians," in *European Conference on Computer Vision*. Springer, 2024, pp. 165–181.

[38] Z. Zhang, T. Song, Y. Lee, L. Yang, C. Peng, R. Chellappa, and D. Fan, "Lp-3dgs: Learning to prune 3d gaussian splatting," *Advances in Neural Information Processing Systems*, vol. 37, pp. 122 434–122 457, 2024.

[39] A. Hanson, A. Tu, G. Lin, V. Singla, M. Zwicker, and T. Goldstein, "Speedy-splat: Fast 3d gaussian splatting with sparse pixels and sparse primitives," in *Proceedings of the Computer Vision and Pattern Recognition Conference*, 2025, pp. 21 537–21 546.

[40] M. Niemeyer, F. Manhardt, M.-J. Rakotosaona, M. Oechsle, D. Duckworth, R. Gosula, K. Tateno, J. Bates, D. Kaeser, and F. Tombari, "Radsplat: Radiance field-informed gaussian splatting for robust real-time rendering with 900+ fps," in *2025 International Conference on 3D Vision (3DV)*. IEEE, 2025, pp. 134–144.

[41] G. Fang and B. Wang, "Mini-splatting2: Building 360 scenes within minutes via aggressive gaussian densification," *arXiv preprint arXiv:2411.12788*, 2024.

[42] Y.-T. Zhan, C.-Y. Ho, H. Yang, Y.-H. Chen, J. C. Chiang, Y.-L. Liu, and W.-H. Peng, "Cat-3dgs: A context-adaptive triplane approach to rate-distortion-optimized 3dgs compression," *arXiv preprint arXiv:2503.00357*, 2025.

[43] Y. Chen, M. Li, Q. Wu, W. Lin, M. Harandi, and J. Cai, "Pegs: Progressive compression of 3d gaussian splatting," *arXiv preprint arXiv:2503.08511*, 2025.

[44] J. Chen, Y. Chen, Y. Zou, Y. Huang, P. Wang, Y. Liu, Y. Sun, and W. Wang, "Megs2: Memory-efficient gaussian splatting via spherical gaussians and unified pruning," *arXiv preprint arXiv:2509.07021*, 2025.

[45] Z. Fan, K. Wang, K. Wen, Z. Zhu, D. Xu, and Z. Wang, "Lightgaussian: Unbounded 3d gaussian compression with 15x reduction and 200+ fps," 2023.

[46] S. Xie, W. Zhang, C. Tang, Y. Bai, R. Lu, S. Ge, and Z. Wang, "Mesongs: Post-training compression of 3d gaussians via efficient attribute transformation," in *European Conference on Computer Vision*. Springer, 2024.

[47] S. Niedermayr, J. Stumpfegger, and R. Westermann, "Compressed 3d gaussian splatting for accelerated novel view synthesis," in *Proceedings of the IEEE/CVF Conference on Computer Vision and Pattern Recognition (CVPR)*, June 2024, pp. 10 349–10 358.

[48] Y. Lee, Z. Zhang, and D. Fan, "Safeguardgs: 3d gaussian primitive pruning while avoiding catastrophic scene destruction," *arXiv preprint arXiv:2405.17793*, 2024.

[49] A. Hanson, A. Tu, V. Singla, M. Jayawardhana, M. Zwicker, and T. Goldstein, "Pup 3d-gs: Principled uncertainty pruning for 3d gaussian splatting," in *Proceedings of the Computer Vision and Pattern Recognition Conference*, 2025, pp. 5949–5958.

[50] Y. Huang, J. Pang, F. Zhu, and D. Tian, "Entropygs: An efficient entropy coding on 3d gaussian splatting," *arXiv preprint arXiv:2508.10227*, 2025.

[51] W. Liu, T. Guan, B. Zhu, L. Xu, Z. Song, D. Li, Y. Wang, and W. Yang, "Efficientgs: Streamlining gaussian splatting for large-scale high-resolution scene representation," *IEEE MultiMedia*, 2025.

[52] T. Müller, A. Evans, C. Schied, and A. Keller, “Instant neural graphics primitives with a multiresolution hash encoding,” *ACM Trans. Graph.*, vol. 41, no. 4, pp. 102:1–102:15, Jul. 2022.

[53] C. Reiser, S. Peng, Y. Liao, and A. Geiger, “Kilonerf: Speeding up neural radiance fields with thousands of tiny mlps,” in *International Conference on Computer Vision (ICCV)*, 2021.

[54] C. L. Deng and E. Tartaglione, “Compressing explicit voxel grid representations: Fast nerfs become also small,” in *Proceedings of the IEEE/CVF Winter Conference on Applications of Computer Vision (WACV)*, January 2023, pp. 1236–1245.

[55] L. Li, Z. Shen, Z. Wang, L. Shen, and L. Bo, “Compressing volumetric radiance fields to 1 mb,” in *Proceedings of the IEEE/CVF Conference on Computer Vision and Pattern Recognition (CVPR)*, June 2023, pp. 4222–4231.

[56] T. Zhao, J. Chen, C. Leng, and J. Cheng, “Tinynerf: towards 100x compression of voxel radiance fields,” in *AAAI’23/IAAI’23/EAAI’23*. AAAI Press, 2023.

[57] D. Rho, B. Lee, S. Nam, J. C. Lee, J. H. Ko, and E. Park, “Masked wavelet representation for compact neural radiance fields,” in *Proceedings of the IEEE/CVF Conference on Computer Vision and Pattern Recognition*, 2023, pp. 20680–20690.

[58] S. Li, H. Li, Y. Liao, and L. Yu, “Nerfcodec: Neural feature compression meets neural radiance fields for memory-efficient scene representation,” in *Proceedings of the IEEE/CVF Conference on Computer Vision and Pattern Recognition*, 2024, pp. 21274–21283.

[59] T. Pham and S. Mandt, “Neural nerf compression,” in *Proceedings of the 41st International Conference on Machine Learning*, 2024, pp. 40592–40610.

[60] S. Lee, F. Shu, Y. Sanchez, T. Schierl, and C. Hellge, “Ecrf: Entropy-constrained neural radiance fields compression with frequency domain optimization,” in *2024 IEEE 26th International Workshop on Multimedia Signal Processing (MMSP)*. IEEE, 2024, pp. 1–6.

[61] L. Wang, Q. Hu, Q. He, Z. Wang, J. Yu, T. Tuytelaars, L. Xu, and M. Wu, “Neural residual radiance fields for streamably free-viewpoint videos,” in *Proceedings of the IEEE/CVF Conference on Computer Vision and Pattern Recognition*, 2023, pp. 76–87.

[62] T. Takikawa, A. Evans, J. Tremblay, T. Müller, M. McGuire, A. Jacobson, and S. Fidler, “Variable bitrate neural fields,” in *ACM SIGGRAPH 2022 Conference Proceedings*, ser. SIGGRAPH ’22. New York, NY, USA: Association for Computing Machinery, 2022.

[63] S. Shin and J. Park, “Binary radiance fields,” in *Proceedings of the 37th International Conference on Neural Information Processing Systems*, ser. NIPS ’23. Red Hook, NY, USA: Curran Associates Inc., 2024.

[64] Y. Chen, Q. Wu, M. Harandi, and J. Cai, “How far can we compress instant-ngp-based nerf?” in *Proceedings of the IEEE/CVF Conference on Computer Vision and Pattern Recognition (CVPR)*, June 2024, pp. 20321–20330.

[65] Z. Wang, S. Wan, and L. Wei, “Local geometry-based intra prediction for octree-structured geometry coding of point clouds,” *IEEE Transactions on Circuits and Systems for Video Technology*, vol. 33, no. 2, pp. 886–896, 2023.

[66] Z. Que, G. Lu, and D. Xu, “Voxelcontext-net: An octree based framework for point cloud compression,” in *Proceedings of the IEEE/CVF Conference on Computer Vision and Pattern Recognition (CVPR)*, June 2021, pp. 6042–6051.

[67] L. Huang, S. Wang, K. Wong, J. Liu, and R. Urtasun, “Octsqueeze: Octree-structured entropy model for lidar compression,” in *2020 IEEE/CVF Conference on Computer Vision and Pattern Recognition (CVPR)*, 2020, pp. 1310–1320.

[68] C. Cao, M. Preda, and T. Zaharia, “3d point cloud compression: A survey,” in *Proceedings of the 24th International Conference on 3D Web Technology*, ser. Web3D ’19. New York, NY, USA: Association for Computing Machinery, 2019, p. 1–9.

[69] R. L. de Queiroz and P. A. Chou, “Compression of 3d point clouds using a region-adaptive hierarchical transform,” *IEEE Transactions on Image Processing*, vol. 25, no. 8, pp. 3947–3956, 2016.

[70] Y. Huang, J. Peng, C.-C. J. Kuo, and M. Gopi, “Octree-Based Progressive Geometry Coding of Point Clouds,” in *Symposium on Point-Based Graphics*, M. Botsch, B. Chen, M. Pauly, and M. Zwicker, Eds. The Eurographics Association, 2006.

[71] K. Zhang, W. Zhu, and Y. Xu, “Hierarchical segmentation based point cloud attribute compression,” in *2018 IEEE International Conference on Acoustics, Speech and Signal Processing (ICASSP)*, 2018, pp. 3131–3135.

[72] S. Schwarz, M. Preda, V. Baroncini, M. Budagavi, P. Cesar, P. A. Chou, R. A. Cohen, M. Krivokuća, S. Lasserre, Z. Li, J. Llach, K. Mammou, R. Mekuria, O. Nakagami, E. Siahaan, A. Tabatabai, A. M. Tourapis, and V. Zakharchenko, “Emerging mpeg standards for point cloud compression,” *IEEE Journal on Emerging and Selected Topics in Circuits and Systems*, vol. 9, no. 1, pp. 133–148, 2019.

[73] M. T. Bagdasarian, P. Knoll, F. Barthel, A. Hilsmann, P. Eisert, and W. Morgenstern, “3dgs.zip: A survey on 3d gaussian splatting compression methods,” 2024.

[74] J. L. Schönberger and J.-M. Frahm, “Structure-from-motion revisited,” in *Conference on Computer Vision and Pattern Recognition (CVPR)*, 2016.

[75] P. Hedman, J. Philip, T. Price, J.-M. Frahm, G. Drettakis, and G. Brostow, “Deep blending for free-viewpoint image-based rendering,” *ACM Transactions on Graphics (SIGGRAPH Asia Conference Proceedings)*, vol. 37, no. 6, November 2018.

[76] A. Knapitsch, J. Park, Q.-Y. Zhou, and V. Koltun, “Tanks and temples: Benchmarking large-scale scene reconstruction,” *ACM Transactions on Graphics*, vol. 36, no. 4, 2017.

[77] Z. Wang, A. Bovik, H. Sheikh, and E. Simoncelli, “Image quality assessment: from error visibility to structural similarity,” *IEEE Transactions on Image Processing*, vol. 13, no. 4, pp. 600–612, 2004.

[78] R. Zhang, P. Isola, A. A. Efros, E. Shechtman, and O. Wang, “The unreasonable effectiveness of deep features as a perceptual metric,” in *2018 IEEE/CVF Conference on Computer Vision and Pattern Recognition*, 2018, pp. 586–595.

[79] Z. Liu, J. Su, G. Cai, Y. Chen, B. Zeng, and Z. Wang, “Georgs: Geometric regularization for real-time novel view synthesis from sparse inputs,” *IEEE Transactions on Circuits and Systems for Video Technology*, pp. 1–1, 2024.

[80] J. Li, J. Zhang, X. Bai, J. Zheng, X. Ning, J. Zhou, and L. Gu, “Dngaussian: Optimizing sparse-view 3d gaussian radiance fields with global-local depth normalization,” *arXiv preprint arXiv:2403.06912*, 2024.



Bert Ramlot received the M.Sc. degree in computer science engineering from Ghent University, Belgium, in 2024, where he is currently pursuing the Ph.D. degree with IDLab, imec. His current research interests are 3D Gaussian Splatting and compression thereof.



Martijn Courteaux received the M.Sc. degree in computer science engineering from Ghent University, Belgium, in 2018, where he is currently pursuing the Ph.D. degree with IDLab, imec, through the financial support of the Research Foundation–Flanders (FWO). His current research interests focus on the modeling and compression of light fields and light-field videos, and are set in the context of statistics, signal processing, and compression.



Peter Lambert (Senior Member, IEEE) is Full Professor at the IDLab of Ghent University – imec (Belgium). He received his Master’s degree in science (mathematics) and in applied informatics from Ghent University in 2001 and 2002, respectively, and he obtained the Ph.D. degree in computer science in 2007 at the same university. His research interests include multimedia signal processing, data compression, computer graphics, XR, and visual communications.



Glenn Van Wallendael (Member, IEEE) obtained the M.Sc. degree in Computer Science Engineering from Ghent University, Belgium in 2008. Afterwards, he obtained the Ph.D. at IDLab, Ghent University, with the financial support of the Research Foundation - Flanders (FWO). Since 2019, he works as a Professor for both Ghent University and imec on topics such as the efficient representation and compression of visual information, including immersive media, 360 degree video, light fields, and virtual reality.